An activatable, cancer-targeted, hydrogen peroxide probe for photoacoustic and fluorescence imaging.

Judith Weber[1,2,3], Laura Bollepalli[1,2], Ana M. Belenguer[3], Marco Di Antonio[3,*], Nicola De Mitri[3], James Joseph[1,2], Shankar Balasubramanian[1,3], Christopher A. Hunter[3], Sarah E. Bohndiek[#1,2].

[1] Cancer Research UK Cambridge Institute, University of Cambridge, Li Ka Shing Centre, Robinson Way, Cambridge, CB2 0RE, U.K.

[2] Department of Physics, University of Cambridge, JJ Thomson Avenue, Cambridge, CB3 0HE, U.K.

[3] Department of Chemistry, University of Cambridge, Lensfield Road, Cambridge, CB2 1EW, U.K.

[#] Corresponding author. *Phone*: +44 1223 337267; *Fax*: +44 1223 337000; *Email*: seb53@cam.ac.uk

* Now at: Chemistry Department, Imperial College London, Molecular Science Research Hub, Wood Lane W12 0BZ, London, UK.

Running Title: Imaging hydrogen peroxide in cancer

Keywords: Near-infrared dye, photoacoustic imaging, fluorescence imaging, oxidative stress, hydrogen peroxide, 2-deoxyglucose.

Word Count: 5258 excluding abstract and references**; Figure Count:** 6

Financial Support: The Bohndiek lab is supported by: the EPSRC-CRUK Cancer Imaging Centre in Cambridge and Manchester (C197/A16465); CRUK (C14303/A17197; C47594/A16267); and the European Union's Seventh Framework Programme (FP7/2007-2013) under grant agreement n° FP7-PEOPLE-2013-CIG-630729. The Balasubramanian lab is supported by: programme grant funding (C9681/A18618) and core funding (C14303/A17197) from Cancer Research UK. MDA is supported by a BBSRC DPF (BB/R011605/1).

Competing Interests: SEB has received research support from iThera Medical GmbH and PreXion Inc, manufacturers of photoacoustic imaging instruments. SB is a founder and shareholder of Cambridge Epigenetix Ltd.

Abstract:

Reactive oxygen species play an important role in cancer, however, their promiscuous reactivity, low abundance and short-lived nature limits our ability to study them in real time in living subjects with conventional non-invasive imaging methods. Photoacoustic imaging is an emerging modality for *in vivo* visualization of molecular processes with deep tissue penetration and high spatio-temporal resolution. Here, we describe the design and synthesis of a targeted, activatable probe for photoacoustic imaging, which is responsive to one of the major and abundant reactive oxygen species, hydrogen peroxide (H_2O_2). This bifunctional probe, which is also detectable with fluorescence imaging, is composed of a heptamethine carbocyanine dye scaffold for signal generation, a 2-deoxyglucose cancer localization moiety and a boronic ester functionality that specifically detects and reacts to H_2O_2. We characterized the optical properties of the probe using absorption, fluorescence and photoacoustic measurements and quantified changes in these properties upon addition of pathophysiological H_2O_2 concentrations. We then evaluated the promise of the probe *in vitro*, including cell uptake and biocompatibility. Importantly, we showed that this probe is suitable for targeted non-invasive, real-time *in vivo* imaging of H_2O_2 in solid tumors.

Significance:

This study presents the first activatable and cancer-targeted hydrogen peroxide probe for photoacoustic molecular imaging, paving the way for visualization of hydrogen peroxide at high spatio-temporal resolution in living subjects

Introduction

Reactive oxygen species (ROS) are generated as a normal by-product of respiration and at low concentrations act as signaling molecules. Oxidative stress arises when the concentration of ROS exceeds the capacity of intracellular antioxidant systems and plays a key role in the progression of a range of pathologies,[1] including cancer, as well as neurodegenerative and cardio-vascular diseases.[2] For example, a sustained oxidative environment can lead to malignant transformation. Once transformed, aberrant cancer cell proliferation and metabolism together with a complex tumor microenvironment leads to very high levels of ROS.[3] Cancer cells must therefore tightly regulate their antioxidant capacity to survive this ROS exposure; the ability to endure prolonged and severe oxidative stress has been strongly associated with cancer aggressiveness and drug resistance.

Our current understanding of how oxidative stress contributes to cancer progression, and whether strategies to abrogate this adaptive response can be used to modify therapy response, are fundamentally limited by a lack of tools with which to study redox processes with sufficient spatio-temporal resolution in living subjects.[4] Fortunately, photoacoustic imaging (PAI) operates on a regime highly suited to meet these needs. PAI is an emerging molecular imaging modality that enables non-invasive, real-time visualization of cellular and molecular processes in living subjects with a spatial resolution of ~100 µm at depths of several centimeters. It is based on the photoacoustic effect, in which acoustic waves are generated in response to the absorption of short light pulses and subsequent tissue heating. Since sound waves are less scattered by biological tissues than photons, this technique bypasses some of the drawbacks of traditional optical imaging techniques and combines the high temporal and spatial resolution of ultrasound with the high contrast of optical imaging.[5]

Optically absorbing chromophores intrinsic to living subjects (e.g. hemoglobin, melanin and lipids) enable PAI to provide structural and functional imaging. A great variety of signaling compounds used as contrast agents for PAI have already been reported to enable PA

molecular imaging, including small molecule near-infrared dyes, inorganic and organic nanostructures.[6] Probes that are targeted and activatable are of particular interest since they preferentially accumulate in a specific tissue type and then elicit a signal change upon binding or interaction with their target biological process. These two features reduce the impact of the physiological background signals and increase the potential for signal quantification. A PAI probe tailored for the detection of ROS in disease must: be non-toxic; avoid promiscuous reactivity at normal physiological ROS concentrations or with multiple ROS; be highly sensitive to the ROS of interest; and accumulate in the tissue of interest to allow disease-specific readout.

In this study, we created the first activatable and cancer-targeted H_2O_2 probe providing dual contrast in photoacoustic and fluorescence imaging that satisfies these criteria. H_2O_2 is a major and abundant ROS with a relatively high chemical stability involved in cell signaling and strikingly increased in cancer cells.[7] There are several reports describing boronic acid/esters as specific masking groups, which are chemoselectively removed by H_2O_2 over competing ROS.[8–10] Based on this foreknowledge, we designed a smart, targeted near-infrared PAI probe composed of: a heptamethine carbocyanine backbone;[11] an aryl boronate ester reactive towards H_2O_2 connected to the dye backbone via a linker structure; and 2-deoxyglucose as a targeting moiety to direct the probe preferentially to cancerous tissue.[12–14] The resulting probe, **JW41**, allows the effective and selective detection of pathological H_2O_2 concentrations via absorption, fluorescence and photoacoustic spectroscopy. Importantly, we demonstrate the ability of the activatable probe to detect tumor specific H_2O_2-levels in a subcutaneous mouse model of breast cancer *in vivo*. Future *in vivo* application of this new targeted, activatable probe could provide unprecedented insight into the role of oxidative stress in cancer at high temporal and spatial resolution in living subjects.

Materials and Methods

Synthesis

The preparation and characterization of **JW35** and **JW41** as depicted in Figure 1 and Supporting Figure 1 are documented in the Supporting Methods.

Optical Characterization

Absorption maxima (λ_{Abs}), emission maxima (λ_{Em}), Stokes shift, molar extinction coefficient (ε), fluorescence quantum yield (Φ_{Fl}) and brightness (B) were determined. Stokes shifts were calculated from the difference of λ_{Em} and λ_{Abs}. ε was determined using the Beer–Lambert law from dilutions of solutions with known concentrations. Φ_{Fl} of **JW41** and **JW35** in water, MeOH and EtOH/H_2O (7/3) were measured at the excitation wavelength of 785 nm and referenced against 1,1′,3,3,3′,3′-Hexamethylindotricarbocyanine iodide (HITC, 252034, Sigma-Aldrich) in MeOH (Φ_{Fl}=0.28)[15]. Discrepancies in absorbance and solvent refractive index were corrected[16]. To assess the optical responses of **JW41** to H_2O_2 the probe was incubated with 100µM H_2O_2 (pH=6.15) and the absorption, fluorescence and PA spectra recorded before and up to 90min after addition of H_2O_2 at either 5min intervals over the whole period or at 1min intervals for the first 10min followed by 5min intervals. **JW41** in water without the H_2O_2 supplement served as control. To prove that the product of the reaction, **JW35**, does not react further, the same measurements were performed with **JW35**. Selectivity to H_2O_2 was confirmed using LCMS (Supporting Methods). All experiments were repeated with n=3 separately prepared probe samples and errors are represented as standard deviations.

To study the photostability of the probes for *in vivo* applications and potential for spectral unmixing, phantoms with defined optical properties closely mimicking the optical properties of biological tissue were fabricated, imaged and analyzed as described previously[17] and further elaborated in the Supporting Methods. Photoacoustic signals were recorded using 25 different excitation wavelengths between 660nm and 900nm.

In vitro cell experiments

The two human adenocarcinoma cell lines MDA-MB-231 (Estrogen Receptor−, ER−) and MCF-7 (Estrogen Receptor+, ER+) were obtained from the Cancer Research UK (CRUK) Cambridge Institute Biorepository Core Facility at the University of Cambridge and mycoplasma tested. The experiments were performed when cells were between passage 22 to 35 for MCF-7 and between passage 30 to 43 for MDA-MB-231. Authentication using Genemapper ID v3.2.1 (Genetica) by STR Genotyping (11/2017) showed exact match with the reference sequence in both cases. Cells were maintained in Dulbecco's Modified Eagle Medium (21885-025, ThermoFisher Scientific) with 10% heat inactivated fetal calf serum (1050064, ThermoFisher Scientific) at 37 °C in 5% CO_2. The cells were routinely subcultured when reaching 85% confluence (1:10 for MCF-7 and 1:20 for MDA-MB-231).

Full details of all *in vitro* experiments can be found in the Supporting Methods. Cellular toxicity of the probes was examined by quantifying cell proliferation and viability via standard MTT (3-(4,5-dimethylthiazol-2-yl)-2,5-diphenyltetrazolium bromide) assay and IncuCyte proliferation assay. GLUT-dependent uptake kinetics and localization of **JW41** as well as **JW35** were examined in MDA-MB-231 and MCF7 cells using standard fluorescent assays and epifluorescent microscopy. The fluorescence of **JW41**/**35** was collected upon excitation at 770nm. Cells were also stained with: MitoTracker Orange (excitation 580nm); LysoTracker green (excitation 490nm) and NucBlue/Hoechst (excitation 365nm). Zen 2.3 (blue edition) was used for image analysis.

In vivo studies

All animal procedures conducted meet the standards required by the UKCCCR guidelines and were performed under the authority of project and personal licenses issued by the Home Office, U.K., reviewed by the Animal Welfare and Ethical Review Board at the CRUK Cambridge Institute. 300,000 MDA-MB-231 cells in a final volume of 100µL of 1:1 DMEM (GIBCO) and matrigel (BD) were inoculated orthotopically in the mammary fat pad of both

flanks of 10 seven-week-old immunodeficient female nude (BALB/c nu/nu) mice (Charles River). All mice were kept with 5R58 diet (PicoLab) in Tecniplast Green Line cages, individually ventilated in 12/12 h ON/OFF light cycles. Tumors were measured externally with Vernier calipers. The probe was injected and the mouse imaged when tumor size was between 0.5 and 1cm diameter. Animals were killed by exsanguination and cervical dislocation as confirmation of death. Tumors, liver, kidney, spleen, heart and brain were collected for *ex vivo* analysis. Afterwards, tumors and livers were divided into 3 parts for histopathology, microscopy and LC-MS/MS analysis. Kidney, spleen, heart and brain were paraffin embedded. One mouse developed only one tumor that could be fully analyzed and one small tumor, which was not analyzed *ex vivo*.

PA *in vivo* imaging

All PA *in vivo* imaging was performed with the photoacoustic imaging system described in Supporting Methods (inVision 256-TF, iThera Medical GmbH) and mice were prepared for imaging following our standard operating procedure[17]. Briefly, <3% isoflurane was used to anesthetize the mice before they were placed in a custom animal holder (iThera Medical), wrapped in a thin polyethylene membrane. A thin layer of ultrasound gel (Aquasonic Clear, Parker Labs) was used to couple the skin to the membrane. The holder was then placed within the PA system and immersed in heavy water maintained at 36°C. The respiratory rate of the mice was maintained in the range of 70–80b.p.m. with 1.5–2% isoflurane concentration for the entire scan time. 5min after the animal was placed into the imaging system, the scan was initialized and the baseline was monitored for further 14min, to stabilize the signal. 14min into the scan 150µL of the probe in saline (9mg/mL; pH=4.93) was injected intravenously in the tail vein for a 20g mouse at a concentration of 150µM for **JW41**, 50µM for **JW35** and 100µM **JW41** + 50µM **JW35** for the 2-1 mixture. Images were acquired at one slice centered on the liver, one slice centered on the kidneys, spleen and liver, and several slices covering the whole length of both tumors in 1-mm steps. Scans were recorded at 21 wavelengths between 660nm

and 900nm with 10 averages (continuous averaging) for up to 50min in 5min intervals. 24h after injection of the probe the mouse was imaged once again.

Image analysis of PA *in vivo* data

The acquired images were reconstructed offline with model-linear reconstruction and analyzed with linear regression multispectral processing (ViewMSOT version 3.8; iTheraMedical). Linear regression was performed with published spectra for oxy- and deoxyhemoglobin as well as **JW41** and **JW35** spectra obtained from our phantom studies. Regions of interest (ROIs) were drawn around the liver, left kidney, spleen and tumors as identified using the hemoglobin signals as an anatomical reference. Reference values from ROIs drawn as indicated were taken in the same anatomical plane. The PA spectra in the imaged organs were generated by averaging the mean pixel signal intensities of each ROI from every section. For the PA tumor spectra, the average of all tumor spectra of each tomographic section was formed. To correct for the intrinsic background signal, the PA signal recorded at t=0 was subtracted from the subsequent images. To monitor the kinetics of the probe in the different organs, the raw mean pixel intensity values at 760nm and 900nm were used and the ratio was formed. To generate the PA signal kinetic plot based on the spectral unmixing data obtained by linear regression, the values obtained before injection of the probe in the ROI were averaged and used as baseline to allow comparison with the 24h time point signal.

***In vivo* fluorescence imaging**

In vivo fluorescence imaging was carried out on a Xenogen IVIS 200 system. The anaesthetized animal was imaged before the injection of the probe and acquiring the PA scans, after the PA image acquisition, then 50-60min post injection of the probe, as well as 24 h post injection. Scans were recorded with filter set 4 using 705–780nm as the excitation passband, 810–885nm as the emission passband and 665–696nm as the background passband. Autofluorescence was corrected by subtracting the background filter image from the primary filter image. ROIs were drawn on the black and white photographic image of the

mouse without displaying the fluorescence signal. The average radiant efficiency obtained in the control region C was subtracted from the average radiant efficiency within the ROI.

Ex vivo characterization

Tumors were divided into 3 parts, which were either mounted on a cork base using optimal cutting temperature solution (VWR Chemicals) and snap frozen in an isopentane bath cooled to -60°C for fluorescence analysis, snap frozen in liquid nitrogen for LC-MS/MS analysis or fixed in neutral buffered 10% formalin (24h) for hematoxylin and eosin (H&E) staining. Livers were divided in 2 parts, one was snap frozen for LC-MS/MS analysis, the other one fixed in neutral buffered 10% formalin (24h) for H&E staining. Formalin fixed, paraffin embedded tumors and livers were sectioned with 3µm and imaged at ×20 magnification using an Aperio ScanScope (Leica Biosystem) scanner. Frozen blocks were sectioned with 6µm thickness. 2 consecutive slices were generated, of which one was stained with H&E. The other section was fixed with 4% PFA for 5min at room temperature, washed carefully twice with PBS, mounted in mounting media with DAPI (ProLong™ Gold Antifade Mountant with DAPI, LifeTechnologies) and scanned using a wide-field fluorescent microscope (Zeiss Axio Observer Z1) with excitation wavelengths centered on 365nm (for DAPI) and on 740nm for **JW41**/**JW35** under a 63x oil-immersion objective lens.

The concentration of the activatable probe **JW41** and its conversion product, **JW35**, in tissue samples were determined by LC-MS/MS against a reference standard solution (Supporting Fig. 2). **JW41** hydrolyses under aqueous, acidic conditions gradually to **JW41**$_{hydrol}$. Thus, **JW35**, **JW41** and **JW41**$_{hydrol}$ were identified from their retention time and from their specific mass transition in multiple reaction monitoring mode (MRM-MS; Supporting Fig. 3). Full details of the preparation of quality control and internal standard solutions, along with details of the MRM-MS can be found in the Supporting Methods.

Statistical analysis

228 Statistical analysis was performed using GraphPad Prism6. Each tumor was considered as
229 an independent biological replicate. All data are shown as mean±SD.

230

Results

Probe design and synthesis. To accurately map cellular redox conditions at depth *in vivo* by means of PAI, a characteristic change in the absorption spectrum in the near-infrared range must be produced upon interaction with the target redox species. We sought to achieve such a characteristic change by combining a near-infrared heptamethine carbocyanine backbone with a linker unit able to elicit a change in the optical properties of the dye backbone upon H_2O_2-specific reaction. Cyanine-based scaffolds with different linker structures were synthesized and investigated for their ability to trigger a signal change (Supporting Fig. 4, Supporting Methods). Our findings encouraged us to proceed with piperazine and an aryl boronate in para position to a benzylic carbamate linkage (Fig. 1, Supporting Fig. 1, Supporting Methods), which promotes the unique H_2O_2-mediated deprotection due to formation of the phenol and subsequent decarboxylation.[18]

Experimentally measured changes in absorption after cleavage of the aryl boronate moiety in dyes with a piperazine linker structure were supported by density functional theory calculations (Supporting Fig. 5, Supporting Methods). These calculations suggest that the absorption change corresponds to a decreased twist [74.0° (**JW41**) vs 23.3° (**JW35**)] in the relative orientation of the two terminal benzoindole moieties going from the capped probe, **JW41,** to the uncapped derivative, **JW35,** with a consequence of improved electron-delocalization. Similar aromatic linkers did not lead to different absorption spectra, which was in accordance with a nearly identical twist (0.3° and 2.10°; Supporting Fig. 5) in the different derivatives.

Photophysical properties. It is an essential requirement for the determination of H_2O_2 that the induced changes in absorption spectra precisely distinguish the capped (**JW41**) and uncapped (**JW35**) probe (Fig. 2; Supporting Table 1). The results suggest that the capped and uncapped probe are clearly distinguishable via absorption (Fig. 2A), fluorescence (Fig. 2B) and PA spectroscopy (Fig. 2C). The absorption and PA maxima of **JW41** and **JW35** appear in the near-infrared region with an offset of 60nm and 80nm respectively. The fluorescence

emission maximum is located at ~825nm for both forms, leading to a large Stokes shift of about 95 nm for **JW41**, affording an increase in signal-to-noise ratio for fluorescence imaging. Although the capped and uncapped probes showed emission maxima at around the same wavelength, the fluorescence intensity of the uncapped probe ($\Phi_{Fl(\mathbf{JW35})}$=0.0123±0.0015) in aqueous environment increased by over 100% relative to the capped probe ($\Phi_{Fl(\mathbf{JW41})}$=0.0063±0.0009), which can be reasoned by photoinduced electron transfer in the case of **JW41**. This is mirrored by the total integrated emission intensity (brightness, B) of the capped probe ($457M^{-1}cm^{-1}$) in water being half the brightness of the uncapped probe ($951M^{-1}cm^{-1}$), with molar extinction coefficients respectively of $\varepsilon_{\mathbf{JW41}(730nm)}$=61,400$M^{-1}cm^{-1}$ and $\varepsilon_{\mathbf{JW35}(790nm)}$=77,450$M^{-1}cm^{-1}$. Additionally, both probes showed promising photothermal stability for in vivo applications (Fig. 2D) compared to IR800CW, a near infrared dye already widely used in PAI.[19,20]

Having identified a clear shift in the absorption spectrum of the uncapped probe, we then assessed the potential of PAI to accurately detect and quantify the relative concentrations of the capped and uncapped probe in tissue mimicking phantoms. The PA spectra of the two probes at 1 μM and the background obtained in a tissue mimicking phantom (Fig. 2D) served as endmembers for spectral unmixing using linear regression, which enabled identification of the capped or uncapped probe in solution (Fig. 2E). The accuracy (% deviation from the known concentration) for identification of the relative concentration in mixtures (**JW35:JW41**; 100:0, 0:225, 66.6:33.3, 50:50, 33.3:66.6) when compared to a reference of 1 μM JW35 was found to be -6.0% and -5.6% for **JW35** and **JW41** respectively across the range of samples tested (Supporting Table 2). These findings illustrate the effective detection and separation of the two probes from each other and the background with a preciseness suited to detect changes in H_2O_2 under pathological conditions.

ROS sensing. The ability of the capped probe, **JW41**, to respond to H_2O_2 with a change in its photophysical properties was next evaluated with absorption, fluorescence and PA spectroscopy following addition of 100μM H_2O_2, a physiologically realistic concentration in a

cellular environment undergoing oxidative stress.[21] A rapid spectral change was observed following the addition of 100μM H_2O_2. The optical absorption peak at 730nm shifted by 60nm to 790nm and the absorbance at 790nm was found to increase by over 45% (Fig. 3A). Similarly, the photoacoustic peak shifted from 705nm to 785nm with an increase of the 785nm signal by 25% (Fig. 3B). Furthermore, the addition of H_2O_2 elicits a prompt increase in the fluorescence signal at 825nm by over 100% (Fig. 3C). The reaction kinetics could be followed with all three modalities, indicating a fast conversion of the capped probe into the uncapped probe over a period of 10 minutes (Fig. 3D). All measurements were cross validated via LC/MS confirming that the signal changes were caused by the conversion of **JW41** to **JW35** (Fig. 3E). These properties were specific to the radical species H_2O_2 with no cross-reactivity observed in a wide range of other radical species using LC/MS with UV monitoring (Fig. 3E). The generation of the different radical species was verified independently using standard methods. As the oxidation reaction is irreversible, this probe records the total H_2O_2 exposure to the system, rather than an equilibrium value.

***In vitro* evaluation.** Both probes showed good stability in plasma at 37°C with no significant formation of degradation product detected after 2h (Supporting Fig. 6A). Protein binding not only influences the optical properties of dyes but also hampers extravasation and hence affects the biodistribution of a contrast agent (e.g. by increasing hepatic clearance). Both **JW35** and **JW41** bound more strongly to protein than a low protein binding dye (IR800CW) but considerably less than a strongly protein binding dye (ICG) (Supporting Fig. 6B).[22]

To establish the toxicity and uptake profiles of the new probe, two breast cancer cell lines, MCF-7 and MDA-MB-231, were used. These two cell lines differ significantly in their ROS production abilities[23] and MDA-MB-231 cells typically express higher levels of *glut1* mRNA than MCF7 cells[24] (Supporting Fig. 6C). The cytotoxicity of the capped and uncapped probe was tested via MTT viability assay and IncuCyte proliferation assay. Neither the capped or uncapped probes showed any significant cytotoxicity over 5 days in the cell lines tested (Fig. 4A, B).

Next, we investigated the cellular uptake of the new probe using the fluorescence capability in microscopy. In cell studies with MCF-7 and MDA-MB-231, addition of 5μM **JW41/JW35** resulted in a rapid cellular uptake already after 15min, with continued increases observed over 4h (Fig. 4C). To more precisely identify the intracellular localization, microscopic examination of live and fixed MDA-MB-231 and MCF7 cells by wide field microscopy were performed. Co-staining with Hoechst for nuclear localization, WGA-AF488 for membrane staining, MitoTracker orange for mitochondrial staining and LysoTracker green for lysosomal staining, suggest that the observed signal from **JW41** and **JW35** can be localized to the cytosol of the cells with no nuclear or cell surface colocalization (Fig. 4D and Supporting Fig. 6D).

Finally, to establish the GLUT targeting ability of the probe and to test whether the cellular uptake is GLUT-mediated, we performed a 12-O-tetradecanoylphorbol-13-acetate (TPA) uptake assay. TPA generates a rapid upregulation of cell surface localization of GLUT1 resulting in an increased glucose uptake.[25] This facilitation of glucose transport resulted in an increase in **JW41** uptake. IR800CW was used as a negative control without targeting moiety and IR800CW-2DG as a positive control.[26] This control pair was chosen due to the similarity in targeting structure, molecular weight and near-infrared absorption / fluorescent signals in the same range as **JW41**. A significant increase in fluorescence occurred for **JW41** and the positive control IR800CW-2DG in both cell lines when treated with TPA, whereas there was no uptake increase observed in cells treated with IR800CW (Supporting Fig. 7). These results support specific recognition of **JW41** by tumor cells via glucose transporters.

***In vivo* evaluation.** The ability to detect the photoacoustic and fluorescence signals of the capped and uncapped probes in living subjects was studied in subcutaneous MDA-MB-231 tumors in nude mice. Initially, the probes were injected into healthy mice (n=2), which were kept alive for a month after injection. No signs of toxicity were observed in these mice.

Next, the biodistribution of a 2:1 mixture of **JW41**-**JW35** injected intravenously was evaluated (Supporting Fig. 8; n=2 mice, n=2 tumors). Spectral unmixing was performed based on the

measured spectra of the probes and published spectra for oxy- and deoxyhemoglobin[27] (Supporting Fig. 8A). Both **JW41** and **JW35** probes could be successfully distinguished from each other and the background enabling visualization. An increase in PA signal intensity as well as a change in the PA spectrum was observed immediately in both the tumors and healthy organs (Supporting Fig. 8B). Analysis of the **JW41:JW35** signal ratio in the liver (the organ with the highest PA signal following injection) shows that the measured ratio was within 11% of the expected 2:1 value (Fig. 2). We also analyzed our time course data using the ratio of the PA signal at 765nm (the isosbestic point of the two probes) to 900nm. The initial uptake of the mixture in tumors and healthy organs remained over the initial imaging session of 30min following injection but was diminished by 24h (Supporting Fig. 8C). The accumulation and retention of the probes was confirmed with fluorescence imaging acquired before probe injection, 1h post injection as well as 24h after injection (Supporting Fig. 8D, E). Furthermore, the control regions of interest (illustrated in Supporting Fig. 8A) show an initial rise in PA signal as the probe mixture circulates in the blood volume of the mouse, but then return to baseline within 15 min (Supporting Fig. 8F).

Having established that **JW35** and **JW41** could be resolved *in vivo*, the capped probe, **JW41**, was injected alone (Fig. 5; n=4 mice, n=7 tumors). An increase in PA signal intensity and change in spectral shape could be observed after injection (Fig. 5A, B). In this case, however, the strong photoacoustic signal seen immediately after injection persisted for 24h in the tumors and liver. In comparison to the mixture injection, this indicates that a specific uptake and retention is seen in the tumors and liver for the capped **JW41** probe and that the uncapped **JW35** probe exhibits faster clearance (Fig. 5C). The specific accumulation and retention of the probe in tumor and liver was confirmed with fluorescence imaging (Fig. 5D, E). Again, the PA signals in the control regions returned to baseline within 15min (Supporting Fig. 9) confirming that the kinetics observed are organ specific. Finally, comparing the time course of the spectrally unmixed signals in the tumor region shows a similar distribution profile to the ratio of the single wavelengths but with a negligible contribution of the capped **JW41** probe by

24h, as might be expected following complete conversion of the capped **JW41** to the uncapped **JW35** (Fig. 5F; Supporting Fig. 10A). The spectral unmixing data for the 2:1 mixture injection (Supporting Fig. 10B) indeed reflects a 2:1 ratio in the healthy organs, although it appears closer to 1:1 in the tumor tissue, suggesting parts of the **JW41** were already converted into **JW35** within the tumor within the first 5min after injection. Nonetheless, comparing the signals of **JW41** and **JW35** in the ROIs of the mice injected with only **JW41** to a 2:1 mixture of **JW41**:**JW35** indicates a conversion of 57±14% of the injected **JW41** into **JW35** (average across 7 tumors; time course data in Supporting Fig. 10). These results suggest a good tumor targeting efficiency and demonstrate the applicability of the probe to undergo conversion *in vivo*.

***Ex vivo* evaluation.** Finally, we sought to confirm the localization and conversion of the probe in the tumors *ex vivo* excised after the 24h imaging time point. Qualitative comparison of H&E stained tumor tissue with the probe fluorescence using wide-field microscopy of consecutive frozen tumor sections (Fig. 6A) suggests that the probe accumulates to a greater extent in non-necrotic areas. Co-staining with DAPI confirmed that the probe is uptaken into the cytosol of the cells *in vivo* as was shown before for *in vitro* conditions (Fig. 6A zoom; Supporting Fig. 11A, B). To verify the conversion of **JW41** into **JW35** *in vivo*, we performed LC-MS/MS analysis of **JW41** and **JW35** in tissue extracts to evaluate the concentration of the probes. **JW35** was detected in all tumors, confirming the successful conversion from **JW41** in those mice that received injection of **JW41** alone (Supporting Fig. 2E). The total probe concentration in the liver calculated by LC-MS/MS combined with multiple reaction monitoring mass spectrometry (MRM-MS) analysis was around 4-fold higher than the probe concentration in the tumors, which corroborates the 4-fold greater PA signal amplitude in the liver compared to the tumor regions observed during *in vivo* imaging. The conversion of **JW41** into **JW35** in mice injected with **JW41** alone was calculated to be 36±4% (Fig. 6B) in tumor tissue, which is somewhat lower than the value estimated using PA spectral unmixing. By contrast, the conversion in the liver tissue was negligible (3±3%). This was expected as the H_2O_2 production

391 in the liver should be relatively small in comparison to the tumor and the PA signals from
392 spectral unmixing are diminished at the 24h time point (Supporting Fig. 10, Supporting Table
393 3). The experiment was also completed for the mice treated with the 2:1 **JW41**:**JW35** mixture.
394 Since the organs were only collected 24h after injection of the probe, the relative amount of
395 **JW35** in the tumors and liver was similar to the mice treated only with **JW41**, with 39±4% in
396 the tumor sections and 7±4% in the liver sections. This is again in line with the PA results,
397 which suggested a faster clearance of **JW35**.

398

Discussion

New methods for the specific detection and quantification of ROS *in vivo* are necessary to advance our understanding of oxidative stress in cancer. Accordingly, we designed a new targeted photoacoustic and fluorescent probe for the detection of H_2O_2 and demonstrated successful application *in vitro* and *in vivo*.

Spectral unmixing of PA images allowed the relative quantification of the concentration of the capped probe, **JW41**, and the H_2O_2-transformed uncapped probe, **JW35**, in tissue mimicking phantoms with accuracies of ~6%. *In vitro* studies showed no significant toxicity and specific uptake of the probe into the cytosol in both MDA-MB-231 and MCF7 cells. The cellular uptake was increased by treating the cells with TPA, suggesting effective GLUT targeting. Intravenous injection of the capped probe, **JW41**, into MDA-MB-231 tumor bearing mice indicated a good *in vivo* biodistribution. Uptake and specific accumulation into the tumors and background accumulation in the liver over 24h were observed in both photoacoustic and fluorescence imaging and no signs of toxicity were observed in mice monitored over 4 weeks. Specific changes in PA spectra enabled spectral unmixing to generate images indicating the relative concentrations of the injected probe, **JW41,** as well the conversion product, **JW35** that were in reasonable agreement with expectation. Histopathological and wide field microscopy-based *ex vivo* examination confirmed heterogenous cytosolic localization of the new probe in tumor sections and indicated a decreased accumulation in necrotic tumor areas. To validate that **JW41** was converted by H_2O_2 into **JW35** in tumor tissue, LC-MS/MS by MRM-MS analysis was performed, suggesting around 4-times higher conversion rate of **JW41** into **JW35** inside the tumors compared to liver tissue, which is to be expected given the high levels of oxidative stress in solid tumors compared to normal tissues.

The vast majority of H_2O_2 responsive probes have been developed for fluorescence or luminescence imaging.[28–31] Unfortunately, all-optical imaging modalities are restricted by light scattering in tissue to superficial depths and have poor spatial resolution. Near-infrared probes

have been developed to improve the depth of penetration by accessing the 'tissue optical window',[32,33] however, the spatial resolution remains low. Conversely, PAI provides whole-body imaging in small animals (~3cm depth) at high spatial resolution (~150um). Prior reports of hydrogen-peroxide responsive PAI used untargeted nanoplatforms,[34–36] which afforded a substantial increase in absorbance upon sensitive and specific reaction with H_2O_2. Yet in all cases, the absorption spectrum itself was unchanged, making it challenging to discern the difference between an organ with higher uptake of the nanoplatform from one with higher H_2O_2 concentration. The nanoplatforms were also relatively large in size (>100nm) and lacked a specific targeting moiety, relying on passive uptake in the disease state of interest. Furthermore, induction of oxidative stress by these nanoplatforms, which has been reported in other nanoparticle studies, was not specifically investigated. Our probe overcomes these limitations as it is based on a small molecule dye, provides a spectral shift in response to H_2O_2 and is targeted to the disease site of interest, which enabled direct hydrogen-peroxide responsive PAI in tumor models.

Despite these promising findings, there are some limitations to the study. The spectral unmixing approach used shows some signal misclassification, which could arise due to changes in the probe spectra under physiological conditions *in vivo* or due to spectral coloring from depth dependent attenuation of shorter wavelengths. Applying a fluence correction to the data may improve the latter. Making structural modifications to the probe to generate narrower peaks and greater spectral differences between the capped and uncapped probe would enable better distinction of the spectra. An alternative approach would be to create an absorbing product from a non-absorbing precursor. Another limitation is our targeting of the probe to cells with increased expression of the GLUT transporters, which can yield off-target uptake under, for example, inflammatory conditions as exhibited in studies with ^{18}F-fluorodeoxyglucose using positron emission tomography.[37] Using a targeting moiety that binds to a molecular marker that is specific to the cancer cells of interest would allow us to study the presence of H_2O_2 while avoiding off-target effects. Finally, we have considered here only

452 average signals across the entire tumor volume. Future studies should explore and validate
453 any heterogeneity in the probe biodistribution and conversion within the tumor.

454 In summary, our results suggest that this probe could enable the physiology and pathology of
455 H_2O_2 to be evaluated in cancer models to provide new insights into oxidative stress biology.
456 Given the recent translation of PAI into early clinical trials and the high biocompatibility of the
457 probe, with further refinement, our approach could pave the way to specific imaging of
458 oxidative stress in solid tumors in patients.

459

460

Acknowledgements

We thank Stefan Morscher, Neal Burton and Katja Haedicke from iThera Medical GmbH for helpful discussions, letting us use their PA spectroscopy set-up and all their great technical and methodical support. We are especially grateful to Joshua Kent, Mike Mitchell, Jane Gray, Ian Hall, Heather Zecchini and Ziqiang Huang from the core facilities of the Cancer Research UK Cambridge Institute for all their great technical support. We thank Hunter's group at the Department of Chemistry for the use of the synthetic laboratory and LCMS facilities. We thank Timothy Witney for helpful advice regarding our in vivo experiments.

Associated Content

Supporting Information accompanies this manuscript. The data supporting this manuscript will be made available online upon publication of the manuscript (DOI TBC).

References

1. Benz, C. C. & Yau, C. Ageing, oxidative stress and cancer: Paradigms in Parallax. *Nat. Rev Cancer* **8**, 875–879 (2008).

2. Pham-Huy, L. A., He, H. & Pham-Huy, C. Free radicals, antioxidants in disease and health. *Int. J. Biomed. Sci.* **4**, 89–96 (2008).

3. Cairns, R., Harris, I. & Mak, T. Regulation of cancer cell metabolism. *Nat Rev Cancer* **11**, 85–95 (2011).

4. Egea, J. *et al.* Corrigendum to “European contribution to the study of ROS: A summary of the findings and prospects for the future from the COST action BM1203 (EU-ROS)” (Redox Biol. (2017) 13 (94–162)(S2213231717303373)(10.1016/j.redox.2017.05.007)). *Redox Biol.* **14**, 694–696 (2018).

5. Ntziachristos, V. Going deeper than microscopy: the optical imaging frontier in biology. *Nat. Methods* **7**, 603–614 (2010).

6. Weber, J., Beard, P. C. & Bohndiek, S. E. Contrast agents for molecular photoacoustic imaging. *Nat. Methods* **13**, (2016).

7. Lisanti, M. P. *et al.* Hydrogen peroxide fuels aging, inflammation, cancer metabolism and metastasis: The seed and soil also needs ‘fertilizer’. *Cell Cycle* **10**, 2440–2449 (2011).

8. Dickinson, B. C., Huynh, C. & Chang, C. J. A palette of fluorescent probes with varying emission colors for imaging hydrogen peroxide signaling in living cells. *J. Am. Chem. Soc.* **132**, 5906–5915 (2010).

9. Miller, E. W., Albers, A. E., Pralle, A., Isacoff, E. Y. & Chang, C. J. Boronate-based

fluorescent probes for imaging cellular hydrogen peroxide. *J. Am. Chem. Soc.* **127**, 16652–16659 (2005).

10. Kuang, Y., Balakrishnan, K., Gandhi, V. & Peng, X. Hydrogen peroxide inducible DNA cross-linking agents: Targeted anticancer prodrugs. *J. Am. Chem. Soc.* **133**, 19278–19281 (2011).

11. Narayanan, N. & Patonay, G. A New Method for the Synthesis of Heptamethine Cyanine Dyes: Synthesis of New Near-Infrared Fluorescent Labels. *J. Org. Chem.* **60**, 2391–2395 (1995).

12. Smith, T. A. D. FDG uptake, tumour characteristics and response to therapy: A review. *Nucl. Med. Commun.* **19**, 97–106 (1998).

13. Vander Heiden, M., Cantley, L. & Thompson, C. Understanding the Warburg effect: The metabolic Requiremetns of cell proliferation. *Science (80-.).* **324**, 1029–1033 (2009).

14. Lucantoni, F., Dussmann, H. & Prehn, J. H. M. Metabolic Targeting of Breast Cancer Cells With the 2-Deoxy-D-Glucose and the Mitochondrial Bioenergetics Inhibitor MDIVI-1. *Front. Cell Dev. Biol.* **6**, 1–12 (2018).

15. Duggan, J. X., DiCesare, J. & Williams, J. F. *New Directions in Molecular Luminescence - Investigations on the use of laser dyes as quantum counters for obtaining corrected fluorescence spectra in the near infrared*. (ASTM International, 1983).

16. Lakowicz, J. R. *Principles of fluorescence spectroscopy*. *Principles of Fluorescence Spectroscopy* (2006). doi:10.1007/978-0-387-46312-4

17. Joseph, J. *et al.* Evaluation of precision in optoacoustic tomography for preclinical imaging in living subjects. *J. Nucl. Med.* **58**, (2017).

522 18. Lo, L.-C. & Chu, C.-Y. Development of highly selective and sensitive probes for
523 hydrogen peroxide. *Chem. Commun. (Camb).* 2728–2729 (2003).

524 19. Dogra, V. *et al.* Photoacoustic imaging with an acoustic lens detects prostate cancer
525 cells labeled with PSMA-targeting near-infrared dye-conjugates. *J. Biomed. Opt.* **21**,
526 066019 (2016).

527 20. Joseph, J. *et al.* Photoacoustic molecular rulers based on DNA nanostructures. 1–15
528 (2017). doi:10.1101/125583

529 21. Halliwell, B., Celement Veronique, M. & Lee, H. L. Hydrogen peroxide in the human
530 body. *FEBS Lett.* **486**, 10–13 (2000).

531 22. Muckle, T. J. Plasma proteins binding of indocyanine green. *Biochem. Med.* **15**, 17–
532 21 (1976).

533 23. Hecht, F. *et al.* Redox homeostasis of breast cancer lineages contributes to
534 differential cell death response to exogenous hydrogen peroxide. *Life Sci.* **158**, 7–13
535 (2016).

536 24. Venturelli, L. *et al.* Glucose is a key driver for GLUT1-mediated nanoparticles
537 internalization in breast cancer cells. *Sci. Rep.* **6**, 1–14 (2016).

538 25. Lee, E. E. *et al.* A Protein Kinase C Phosphorylation Motif in GLUT1 Affects Glucose
539 Transport and is Mutated in GLUT1 Deficiency Syndrome. *Mol. Cell* **58**, 845–853
540 (2014).

541 26. Kovar, J. L., Volcheck, W., Sevick-Muraca, E., Simpson, M. a. & Olive, D. M.
542 Characterization and performance of a near-infrared 2-deoxyglucose optical imaging
543 agent for mouse cancer models. *Anal. Biochem.* **384**, 254–262 (2009).

544 27. Optical properties spectra. Oregon Medical Laser Centre website.

http://omlc.org/spectra/

28. Lin, V. S., Dickinson, B. C. & Chang, C. J. Boronate-Based Fluorescent Probes: Imaging Hydrogen Peroxide in Living Systems. *Methods Enzymol.* **526**, 19–43 (2013).

29. Van de Bittner, G. C., Dubikovskaya, E. A., Bertozzi, C. R. & Chang, C. J. In vivo imaging of hydrogen peroxide production in a murine tumor model with a chemoselective bioluminescent reporter. *Proc. Natl. Acad. Sci. U. S. A.* **107**, 21316–21 (2010).

30. Jiang, X. *et al.* Challenges and Opportunities for Small-Molecule Fluorescent Probes in Redox Biology Applications. *Antioxid. Redox Signal.* **29**, 518–540 (2018).

31. Su, Y., Song, H. & Lv, Y. Recent advances in chemiluminescence for reactive oxygen species sensing and imaging analysis. *Microchem. J.* **146**, 83–97 (2019).

32. He, Y. *et al.* A near-infrared fluorescent probe for detection of exogenous and endogenous hydrogen peroxide in vivo. *Dye. Pigment.* **168**, 160–165 (2019).

33. Xiong, J. *et al.* An acetate-based NIR fluorescent probe for selectively imaging of hydrogen peroxide in living cells and in vivo. *Sensors Actuators B Chem.* **288**, 127–132 (2019).

34. Jung, E. *et al.* Molecularly Engineered Theranostic Nanoparticles for Thrombosed Vessels: H2O2-Activatable Contrast-Enhanced Photoacoustic Imaging and Antithrombotic Therapy. *ACS Nano* **12**, 392–401 (2018).

35. Chen, Q. *et al.* H2O2-responsive liposomal nanoprobe for photoacoustic inflammation imaging and tumor theranostics via in vivo chromogenic assay. *Proc. Natl. Acad. Sci.* **114**, 5343–5348 (2017).

36. Gao, W. *et al.* A Redox-Responsive Self-Assembled Nanoprobe for Photoacoustic

Inflammation Imaging to Assess Atherosclerotic Plaque Vulnerability. *Anal. Chem.* **91**, 1150–1156 (2019).

37. Zhuang, H. *et al.* Dual Time Point 18F-FDG PET Imaging for Differentiating Malignant from Inflammatory Processes. *J Nucl Med* **42**, 1412–1417 (2001).

Figure legends

Figure 1. **Overview of the smart, targeted hydrogen peroxide probe for photoacoustic and fluorescence imaging**. The capped near-infrared probe (**JW41**) exhibits an increased accumulation in tumor tissue and an H_2O_2-dependent change in its photophysical properties once uncapped (**JW35**).

Figure 1

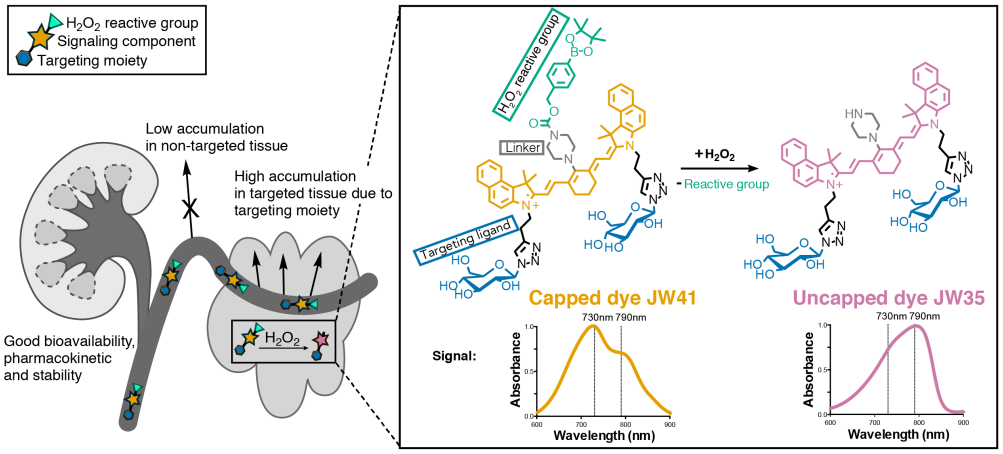

Figure 2. **Optical and optoacoustic properties of the capped (JW41) and uncapped (JW35) probes.** (A) Absorption, fluorescence (excitation λ = 740 nm) and photoacoustic spectra of the capped (**JW41**, 10 µM) and uncapped (**JW35**, 10 µM) probe in water along with photostability data. Photoacoustic spectra were recorded in the tissue mimicking phantom shown in (B). Photostability of 2.5 µM probe solutions was evaluated in tissue mimicking phantoms under continuous laser exposure showing comparable performance to a widely used commercial dye. (B) Schematic illustration of experimental set up for phantom experiments (top) and resulting PA image of the tissue mimicking phantom (bottom) with regions of interest used for analysis illustrated. The normalized PA spectra shown form the foundation for subsequent spectral unmixing. (C) Phantom images containing straws filled with different aqueous **JW41**-**JW35** mixture solutions with adjacent results from spectral unmixing (see also Supporting Table 2). The weights contributed by the **JW41** and **JW35** spectra to

each straw signal are plotted relative to a reference straw (1) containing 1 μM **JW35**. The **JW35:JW41** mixtures tested were 0:225 (top left), 66.6:33.3 (top right), 50:50 (bottom left) and 33.3:66.6 (bottom right).

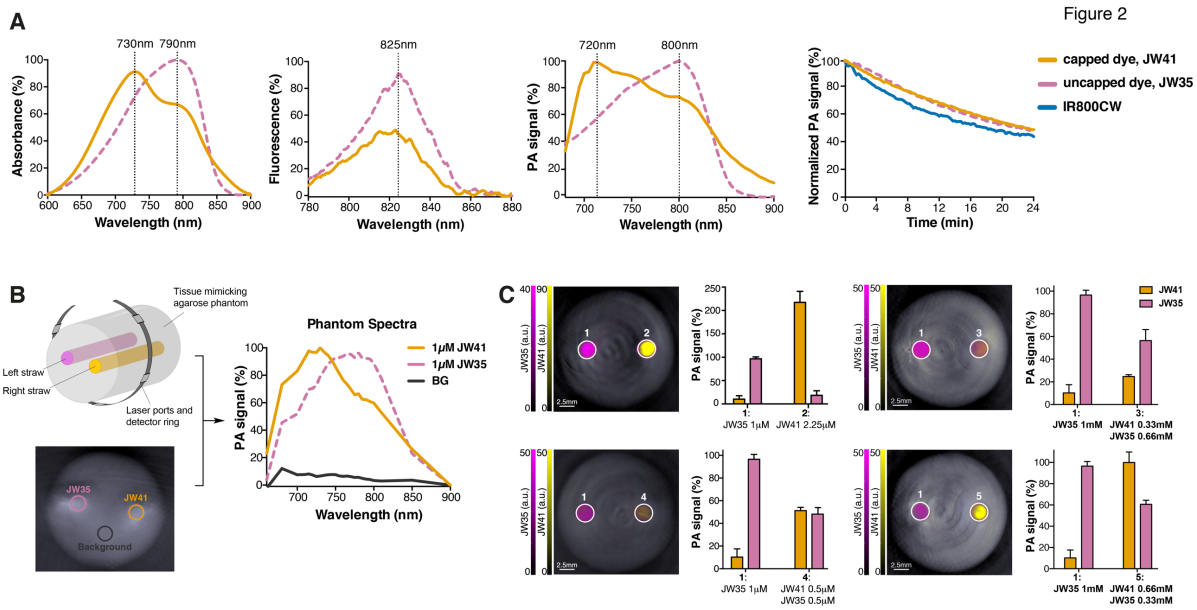

Figure 3. **H_2O_2 reactivity and specificity.** Reaction kinetics of the capped probe (**JW41**; 10 µM) with H_2O_2 (100 µM) could be monitored via absorption (A), photoacoustic (B) and fluorescence (C) spectroscopy. The change in peak absorbance at 730 nm and 790 nm was used to generate the reaction progress curve (D). Data were acquired in water at 25 °C and repeated three times. HPLC-UV monitoring at 750 nm of the response of **JW41** (10 µM) towards different ROS (E) after 60 min ([ROS] ~ 100 µM) shows good specificity. **JW35** (10 µM) was used as endpoint-reference. It should be noted that **JW41** partially hydrolyzes to the corresponding boronic acid (**JW41$_{hydrol.}$**) under aqueous conditions. However, this does not significantly affect the optical properties of the probe.

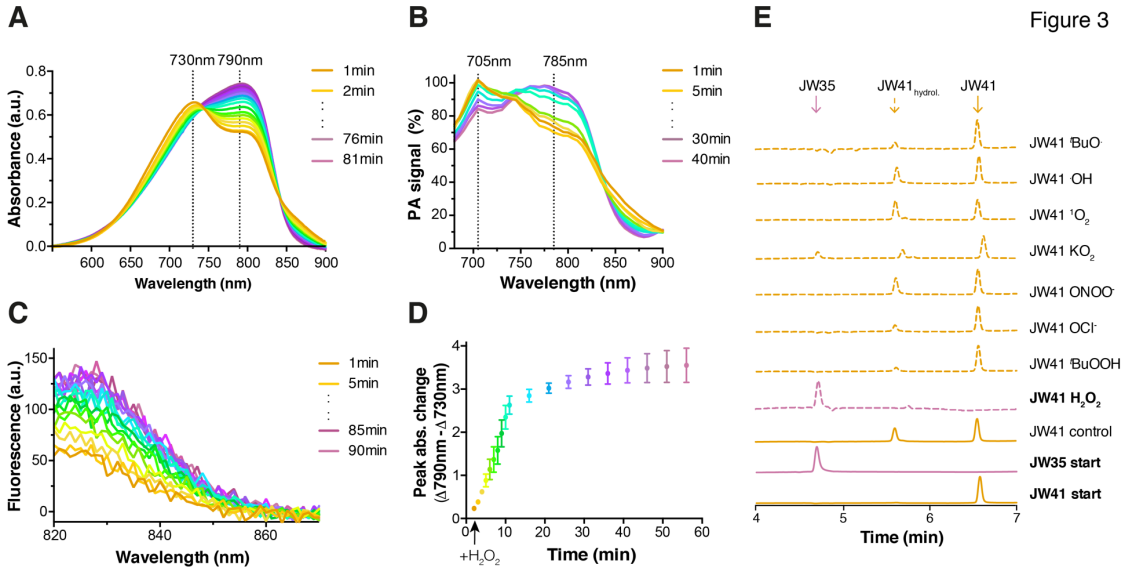

Figure 4. ***In vitro*** **characterization of JW41 and JW35 in MDA-MB-231 and MCF7 cells**. (A) Incubation with 5 µM **JW41**/**JW35** showed negligible impact on cell proliferation. ICG (5 µM) was used as FDA approved control dye, H_2O_2 (1 mM) as toxic control compound and DMF (0.5 %) to correct for possible effects of the solvent used in preparation of the dye stocks. The substances were added 24 h after the cells were seeded. Statistical significance was assessed by 2way ANOVA (n = 4); ****p<0.0001; *p>0.024. (B) Cell viability was tested by MTT assay. Cells were incubated with 5 µM of **JW41**, **JW35**, ICG or 0.5% DMF for 8 h (n = 4). 0.5% DMF was used to correct for the toxicity caused by the solvent of the dyes stock solutions, ICG was

included as a negative reference being an FDA approved dye and 1 mM H_2O_2 as a positive reference causing cell death. (C) Cellular uptake of 2.5 µM **JW41** and **JW35** in MDA-MB-231 and MCF7 cells was measured at the indicated time points (n = 3). (D) Widefield fluorescence images of fixed MDA-MB-231 and MCF7 cells stained with **JW41**/**JW35** (red; 2.5 µM, 60min before fixation), WGA-AF488 (green; 5 µg/mL; 10 min after fixation) and Hoechst (blue; 5 µg/mL; 10 min after fixation) indicates intracellular uptake and cytosolic localization.

Figure 4

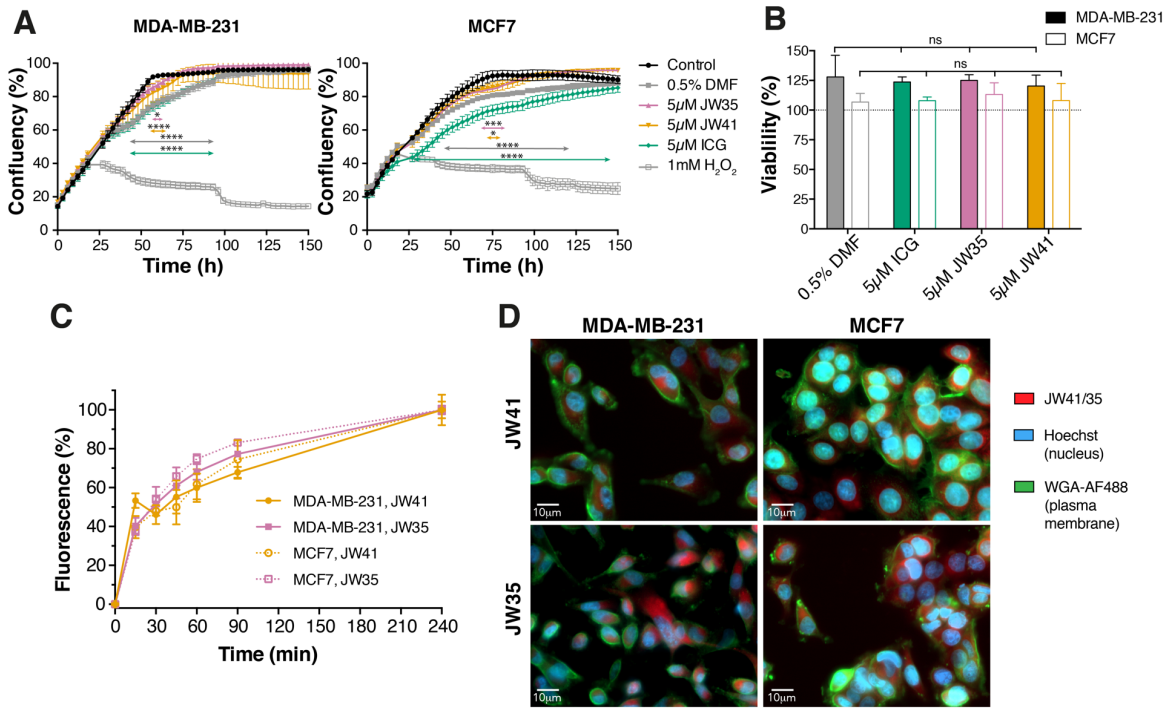

Figure 5. ***In vivo*** **characterization of JW41 in subcutaneous MDA-MB-231 tumors in nude mice. (**A) Representative PAI slice through MDA- MB-231 tumors (top row) and kidney, spleen and liver (bottom row) before and 15-20 min after injection of **JW41**. The regions of interest (ROIs) are indicated with white borders (LT = left tumor, RT = right tumor, L = liver, S = spleen, K = kidney, C = control region). The signal of **JW41** is shown in yellow, the signal of the **JW35** in magenta. (B) Changes in the PA spectra and an increase in the PA signal between 700 and 810 nm were detected in the ROIs upon injection of **JW41**. Representative graphs for tumor (top row) and liver (bottom row) are presented. (C) The time course of the total probe signal at the isosbestic point of the capped and uncapped probe spectra (765 nm) relative to a long wavelength that shows negligible absorption is illustrated in tumors and healthy organs up to 24 h after injection. (D) Fluorescence images before, 1 h and 24 h post injection of **JW41**. (E) The time course of fluorescent radiant efficiency in the tumors and liver upon JW41 injection (values from the control region, C, were used for background correction). (F) The time course of PA signal change evaluated using spectral unmixing.

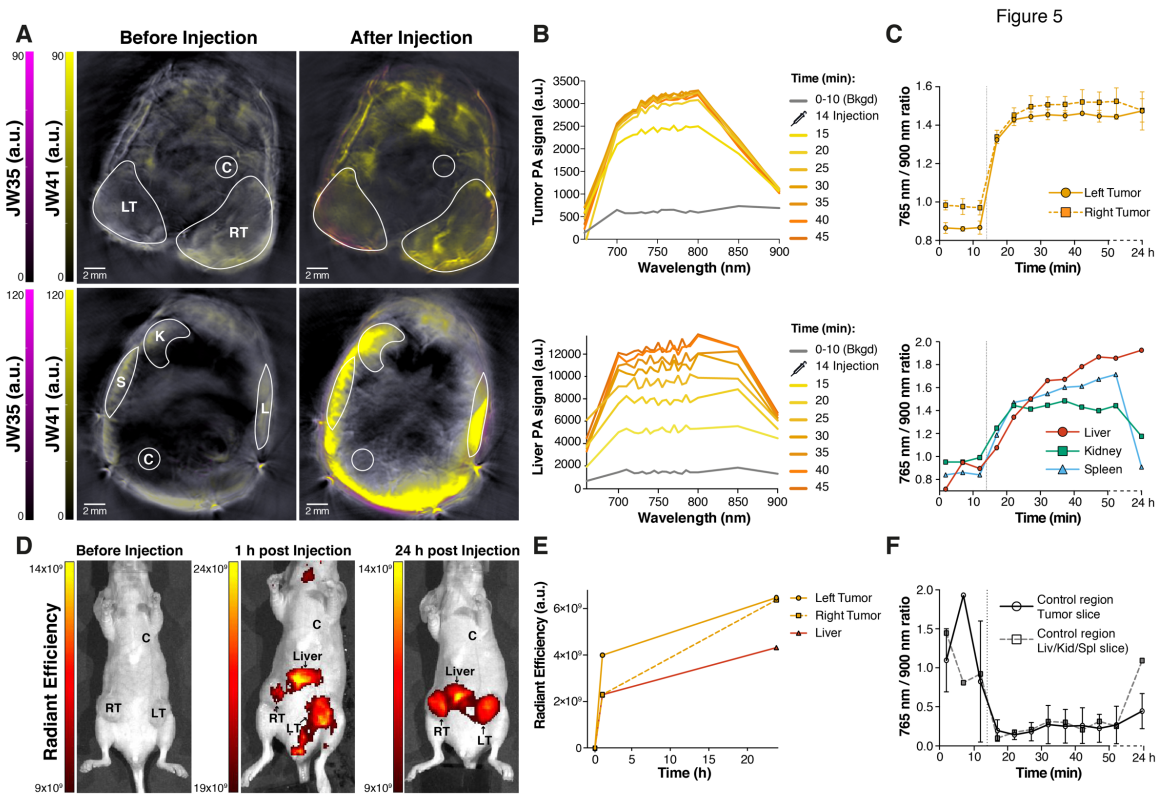

Figure 6. ***Ex vivo* characterization of JW41 and JW35**. (A) Representative H&E stained section of a frozen MDA-MB-231 tumor from a mouse injected with **JW41** compared to a representative widefield fluorescence image of the consecutive tumor section after formaldehyde fixation and staining with DAPI (blue). The necrotic area is indicated with the white line. Magnification of the widefield images allowed qualitative confirmation of the localization of the probe signal into the cytosols of the cells. (B) Quantification of the amount of **JW41** present in the tumors and livers being converted into **JW35** based on LC-MS/MS by MRM-MS analysis (conversion rate in mole %).